Circulation, Heat, and Freshwater Transport at 36°N in the Atlantic

ELAINE L. MCDONAGH, PAULA MCLEOD, BRIAN A. KING, AND HARRY L. BRYDEN

Ocean Observing and Climate Research Group, National Oceanography Centre, Southampton, Southampton, United Kingdom

SINHUÉ TORRES VALDÉS

Ocean Biogeochemistry and Ecosystems Research Group, National Oceanography Centre, Southampton, Southampton, United Kingdom

(Manuscript received 4 November 2008, in final form 20 May 2010)

ABSTRACT

In May and June 2005, a transatlantic hydrographic section along 36°N was occupied. A velocity field is calculated using inverse methods. The derived 36°N circulation has an overturning transport (maximum in the overturning streamfunction) of 16.6 Sv (1 Sv $\equiv 10^6$ m^3 s^{-1}) at 1070 m. The heat transport across the section, 1.14 $\pm$ 0.12 PW, is partitioned into overturning and horizontal heat transports of 0.75 and 0.39 PW, respectively. The horizontal heat flux is set by variability at the gyre rather than by mesoscale. The freshwater flux across the section is 1.55 $\pm$ 0.18 Sv southward based on a 0.8-Sv flow from the Pacific through the Bering Strait at a salinity of 32.5 psu. The oceanic divergence of freshwater implies a net input of freshwater to the ocean of 0.75 Sv over the North Atlantic and Arctic between 36°N and the Bering Strait. Most (85%) of the recently ventilated upper North Atlantic Deep Water (water originating in the Labrador Sea) transport across the section occurs in the deep western boundary current rather than being associated with an interior pathway to the west of the mid-Atlantic ridge.

1. Introduction

At present there is uncertainty as to the size of the poleward ocean heat transport across 36°N in the Atlantic. Roemmich and Wunsch (1985, hereafter ROW) and Rintoul and Wunsch (1991, hereafter RIW) each used the 1981 24° and 36°N transatlantic sections with a similar inverse methodology to determine the same heat transport across 24°N of 1.2 PW, but different heat transports across 36°N of 0.8 (ROW) and 1.3 PW (RIW). Global analyses of Talley (2003) and Macdonald (1998) give heat fluxes at 36°N of 0.86 PW and 1.01 $\pm$ 0.26 PW using the same data at 36°N as RIW and ROW. Macdonald (1998) used 15 hydrographic sections, distributed globally and combined in a box inverse calculation. In the North Atlantic, the global analysis of Talley (2003) was based on the flow fields determined by Reid (1994), using a single level of no motion, close to the 36.8-σ_2 level. Koltermann et al. (1999) calculated heat fluxes across 36°N between 0.47 and 1.29 PW, the highest of these values—1.29 $\pm$ 0.17 PW—used the 1981 data used by the other studies mentioned earlier. Using historical hydrographic data, Sato and Rossby (2000) calculate a mean heat flux at 36°N of 1.2 $\pm$ 0.3 PW. Thus, there is variability in the previous estimates of the oceanic heat flux across 36°N in the Atlantic; even when only estimates from the 1981 data are considered, the range is 0.8–1.3 PW. This range is straddled by the analyses of ROW and RIW. The principal difference between these two analyses was the amount of smoothing used. RIW argue that eddy fluxes are responsible for the higher northward heat transport that they derive and that these fluxes account for the additional 0.5 PW (40% of their total heat transport).

Whether the ocean heat transport grows from 1.2 to 1.3 PW from 24° to 36°N or whether it shrinks from 1.2 to 0.8 PW, it is important in terms of the global distribution of poleward ocean heat transport and in terms of constraining flux climatologies (e.g., Grist and Josey 2003). Some analyses (e.g., Trenberth and Caron 2001) suggest that ocean heat transport peaks in the tropics and decays quickly with latitude, so that the ocean transport is minor compared with atmospheric transport at 35°N. Air–sea flux climatologies on the other hand suggest that

Corresponding author address: Elaine McDonagh, National Oceanography Centre, Southampton, European Way, Southampton SO14 3ZH, United Kingdom.
E-mail: elm@noc.soton.ac.uk

DOI: 10.1175/2010JPO4176.1

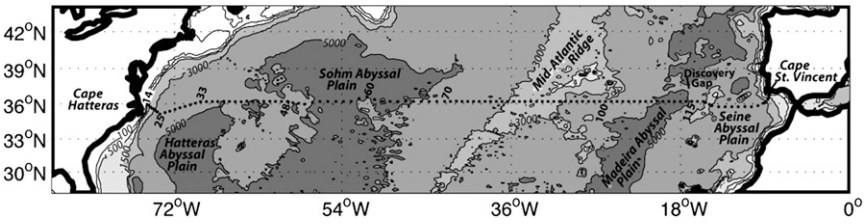

FIG. 1. Transatlantic hydrographic section occupied during CD171 made up of 119 CTD stations numbered 14–21, 24–49, 51–97, and 100–137.

ocean heat transport peaks at a latitude of 30°–35°N (Fig. 4 in Grist and Josey 2003). Thus, determining ocean heat transport at 36°N in the Atlantic has important implications for the ocean's role in climate. In addition, air–sea heat exchange estimates are ambiguous for the region between 24° and 36°N; this is due to uncertainties in the large heat losses to the atmosphere over the Gulf Stream and the extent to which they are balanced by oceanic heat gain over the mid-ocean region between 24° and 36°N (Josey et al. 1999). Identifying the amount of heat gained or lost by the ocean between 24° and 36°N is an important constraint in establishing possible biases in the flux climatologies (Grist and Josey 2003).

The requirement for accurate direct estimates of oceanic freshwater fluxes follows many of the same arguments as for heat fluxes, except the requirement is more acute. Surface freshwater fluxes in climatologies are less well determined than heat fluxes (Taylor 2000). Direct estimates of the freshwater fluxes are less often reported than heat fluxes. For instance RIW and ROW do not report the freshwater fluxes for their circulations. The only estimates of freshwater fluxes at 36°N are from Talley (2008) and Dobroliubov (1997; as reported by Wijffels 2001) who, using the 1981 data, calculate net freshwater inputs to the ocean of 0.33 and 0.49 Sv (1 Sv $\equiv 10^6$ m^3 s^{-1}), respectively, between 36°N and the Bering Strait. The freshwater flux from the North Atlantic is important globally and locally. Regions of freshwater loss contribute to the densification of the upper layers that preconditions the North Atlantic for deep-water formation that constitutes the deep limb of the Atlantic meridional overturning circulation. When analyses similar to that of Grist and Josey (2003) are undertaken for correction of freshwater flux climatologies, then direct estimates of oceanic freshwater fluxes will be crucial.

Here we present a new transatlantic hydrographic section at 36°N, occupied in 2005 on the RRS *Charles Darwin* (CD171; McDonagh et al. 2007). Station 14, the western limit of the section, was occupied on 8 May 2005, and station 137, the eastern limit, was occupied on 12 June. This was the first occupation of the 36°N section with full-depth acoustic current profiling. In this paper a transport field is derived for the 2005 data at 36°N and discussed in terms of the water masses encountered on the section. Heat and freshwater transports for this transport field are quantified.

2. The data

The transatlantic section occupied during CD171 consisted of 119 CTD stations between Cape Hatteras, United States, and Cape St. Vincent, Portugal (Fig. 1), beginning and ending in approximately 100 m of water. CTD stations had a nominal separation of 55 km (30 nautical miles) but were more closely spaced at the western and eastern boundaries. The horizontal resolution during CD171 was therefore comparable to that of the 1981 section, which employed 103 stations, and it is appropriate to make direct comparisons between the two sections and between derived quantities such as heat and freshwater fluxes.

During CD171 $CTDO_2$ data were collected using a Sea-Bird Electronics 911plus CTD. Oxygen and salinity (S) data from the CTD were calibrated against bottle samples, usually 24 per cast. Temperature, salinity, and oxygen data at 2 dbar were interpolated onto a 20-m grid using linear regression over ± 10 m (Figs. 2a–c). Silicate measurements determined using an autoanalyser were interpolated in the vertical on neutral density onto the same 20-m grid as the $CTDO_2$ data (Fig. 2d). Details of data collection, analysis, and processing are given in the cruise report (McDonagh et al. 2007).

One downward-looking RD Instruments Workhorse 300-kHz (WH300) ADCP was mounted on the rosette. Near to the seabed (within ~200 m), the built-in lowered ADCP (LADCP) mode of the WH300 provided bottom-velocity data (from internal processing of the water-track ping) that could be combined with the water-track data to generate a short profile segment of absolute water velocities, without reference to external navigation. For each station the sequence of WH300 pings gathered in this way were combined into a single profile segment of near-bottom absolute velocities that we refer to as the bottom-tracked profile (BTADCP) for that station. All

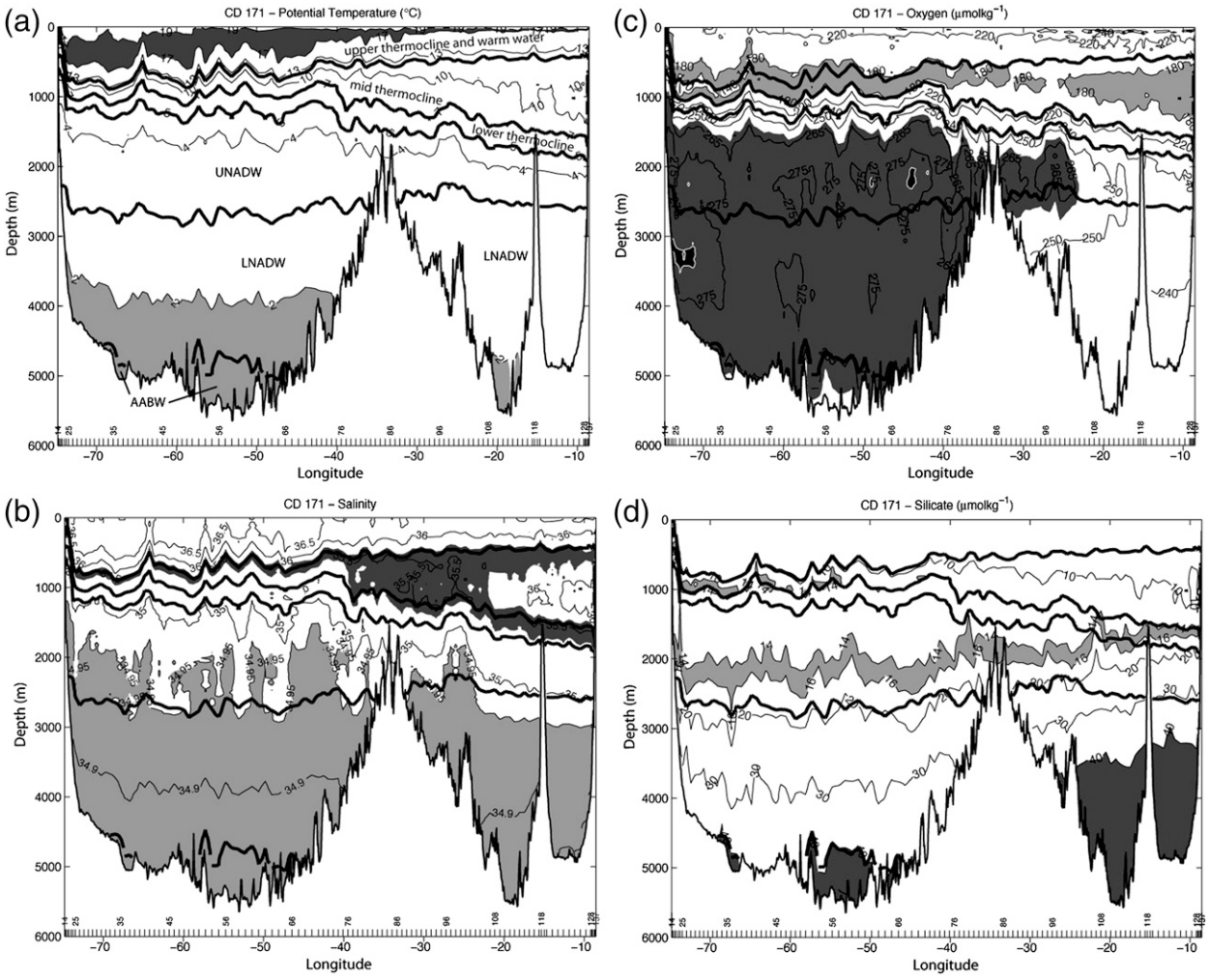

FIG. 2. CD171 contour plots of (a) θ, (b) salinity (S), (c) dissolved oxygen, and (d) silicate. The bold lines represent the 1.8°, 3°, 5°, 7°, and 12°C contours. Water masses between these θ surfaces are labeled in (a) and described in section 4. Intervals of particular interest have been shaded: (a) $\theta < 2$°C is light gray and 17°C $< \theta <$ 19°C is dark gray; (b) $S < 34.95$ is light gray and $35.3 < S < 35.7$ is dark gray; (c) 140 μmol kg^{-1} $< O_2 <$ 180 μmol kg^{-1} is light gray, 260 μmol kg^{-1} $< O_2 <$ 280 μmol kg^{-1} is dark gray, and $O_2 >$ 280 μmol kg^{-1} is black (A white contour marks the 280 μmol kg^{-1} isopleth); and (d) 14 μmol kg^{-1} $<$ silicate $<$ 16 μmol kg^{-1} is light gray, and silicate $>$ 40 μmol kg^{-1} is dark gray.

ADCP measurements used here were detided using the Egbert TPXO6.2 barotropic tidal model (Egbert et al. 1994).

3. Deriving the circulation at 36°N

A geostrophic velocity field is constructed using the density field from CTD measurements. ADCP data are used to provide a level-of-known motion for the initial velocity field (section 3a). Singular value decomposition (SVD) is used to derive a reference-level velocity from an underdetermined inverse problem (Wunsch 1996). The inverse methodology combines the velocity field with circulation and net salinity and silicate flux constraints (summarized in Table 1 and detailed in section 3b). As the system is underdetermined, we must choose one of an infinite number of solutions. We choose the solution that is "closest" (it formally has the smallest L2 norm) to the initial field. Thus, it is important that the initial field is as realistic as possible.

a. Initial velocity field

Our preferred reference velocity for the initial geostrophic field is given by the mean offset to the BTADCP at the station pair adjacent to the geostrophic profile. Spurious BTADCP velocities at stations 58, 66, 82, 94, and 128 were omitted from this process. The reference velocities affected by these omissions were offset to the

TABLE 1. Transport constraints and their values in the initial and solution fields. Uncertainties and posterior errors are given for the constraint and solution fields, respectively. Positive transports are toward the north of the section.

Constraint	Definition	Initial	Constraint	Solution
Net salinity (Sv psu)	All station pairs and all depths on the section	−26	−26 ± 5	−26.44 ± 5
Gulf Stream (Sv)	0–2000 m, station pairs 7:11	66.6	66.6 ± 17.3	67.2 ± 17.2
Discovery Gap (Sv)	Cooler than $\theta = 2.05$°C. Station pairs 87:99	−3.0	0.3 ± 0.5	−0.5 ± 0.5
Seine Abyssal Plain (Sv)	Deeper than 3900 m, station pairs 102:110	0.5	0 ± 0.5	−0.6 ± 0.5
Net silicate (kmol s^{-1})	All station pairs and all depths on the section	206	−20 ± 30	10 ± 30

retained BTADCP profile in the pair. Using the convention that positive (negative) fluxes and velocities are northward (southward), we include a −2-Sv Ekman flux (from mean Hellerman and Rosenstein 1983 winds) distributed evenly along the section over the top 20 m. The last element in the initial velocity field was an offset of -0.276 cm^{-1} across the whole section, so that there was a net salinity flux of −26.0 Sv psu across the section in the initial field. This salinity flux is discussed in detail in the next section. The velocity structure added by the BTADCP is shown in Fig. 3. We represent this structure as the velocity at the bottom and note the coherence in this velocity field [crosses (x) in Fig. 3c]. The largest features in the initial field are at the western and eastern boundaries associated with those current systems, and in the mesoscale features centered at 64° and 55°W (Fig. 3c). The magnitude of the shear in the deep water is represented by the velocity at the bottom relative to 3000 m (thin line in Fig. 3b). This line would be the bottom velocity if 3000 m had been used as a level of no motion of this dataset. This depth (3000 m) has been used as a traditional level of no motion for this section (e.g., in RIW). We note that the bottom velocity relative to 3000 m has shorter space scales than the initial velocity at the bottom. It also does not include several of the features we expect to see on this section at the western boundary, the deep western boundary current (DWBC), northward accumulation of the Gulf Stream, and at the eastern boundary northward-flowing Mediterranean water.

The initial velocity field based on the BTADCP gave net fluxes in layers that agreed with our knowledge of the water mass circulation, for example, northward-flowing bottom and thermocline water and southward-flowing deep water (Table 2). For comparison, two velocity fields were constructed in the same way as our initial field but using a level of no motion at 3000 m and then one at $\sigma_2 = 36.8$ as the first stage instead of BTADCP (Table 2). These two reference levels were used as the basis of RIW's and ROW's initial fields, respectively. The layer transports given by these two reference levels are also reasonable (northward-flowing thermocline water and southward-flowing deep water) except in the bottom water, where the flow is very close to 0 (0.1 Sv for $\sigma_2 = 36.8$ reference) or slightly southward (−0.5 Sv for 3000-m reference). At 32°S in the Indian Ocean, McDonagh et al. (2008) found that the inclusion of ADCP data to reference the initial geostrophic field gave a more realistic flow field than that given by a single level of no motion, particularly in the bottom water. The same is the case here.

b. Constraints and weighting

Five constraints are applied to the system (Table 1). The net salinity transport across the section is constrained to be −26 ± 5 Sv psu. This is based on a Bering Strait throughflow of 0.8 Sv at an average salinity of 32.5 (Coachman and Aagaard 1988). The uncertainty for this constraint is based on a 20% uncertainty in annual mean volume transports calculated in the Bering Strait (Woodgate et al. 2005). The uncertainty in the annual

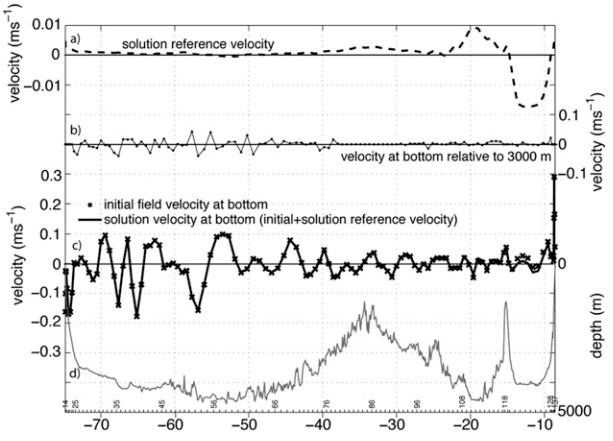

FIG. 3. (a) The solution reference velocity (scale at left). Notice that the dashed line is on a different scale to the other velocity fields. (b) The thin line shows the geostrophic velocity at the bottom relative to 3000 m (scale at right); this is a measure of deep shear and is 0 m s^{-1} if the bottom is shallower than 3000 m. (c) Crosses indicate the bottom velocity in the initial velocity field informed by the ADCP data. The solid bold line indicates the bottom velocity for the final velocity field. The bold line is the sum of the initial field (crosses) plus the solution reference velocity [dashed line in (a); scale at left]. (d) The gray line indicates the section bathymetry (scale at right). Station positions and numbers are indicated on the bottom axis.

TABLE 2. Net transport in potential temperature layers (Sv) for two historically used reference levels (3000 m and $\sigma_2 = 36.8$), the initial velocity field, and the solution velocity field.

	Layer (°C)	3000-m reference	$\sigma_2 = 36.8$ reference	Initial	Solution
Thermocline water	>12	11.43	8.87	11.68	12.87
	7–12	2.28	4.45	11.30	9.25
	5–7	1.53	0.35	2.44	2.68
Deep water	3–5	−4.34	−7.35	−21.89	−19.29
	1.8–3	−11.57	−7.57	−9.78	−11.74
Bottom water	<1.8	−0.53	0.12	4.67	4.68
	Total	−1.19	−1.12	−1.59	−1.55

mean salinity is ~1% and is insignificant compared with the transport uncertainty.

We constrain the Gulf Stream transport to 66.6 ± 17.3 Sv. This is the value of transport in the initial field. This transport is consistent with the mean transport and along-stream growth rate [87.8 ± 17.3 and 15.4 Sv $(100\ \text{km})^{-1}$] from the Pegasus profiler measurements of Halkin and Rossby (1985) approximately 100 km downstream of our Gulf Stream measurements. The uncertainty in the Gulf Stream transport is set equal to the variability calculated using the repeat Pegasus measurements on the nearby line (Halkin and Rossby 1985).

We apply two constraints to the bottom water east of the mid-Atlantic ridge (MAR). The first, a northward flow of 0.3 Sv deeper than the 2.05°C potential temperature (θ) contour, is based on the measurements of Saunders (1987) in Discovery Gap. The 3900-m isobath is closed to the north of this section in the Seine Abyssal Plain. Thus, we constrain a 0-Sv net volume flux to the water deeper than 3900 m in the Seine Abyssal Plain. Each of these bottom water constraints is assigned an uncertainty of 0.5 Sv.

The final constraint is the net silicate flux across the section. To allow silicate concentrations to be used as a constraint on the inversion, we need to establish independently the likely size of the flux across the section. The simplest way to do this is to evaluate the net sinks and sources of silicate to the Atlantic Ocean between the 36°N section and the Bering Strait, where the silicate transport is well constrained (Coachman and Aagaard 1988; Lavin et al. 2003; Mathis et al. 2007).

Silicate exists in both dissolved and particulate forms. Some particulate silicate sinks to the ocean floor and is buried with a fraction of this burial reentering the water column from the sediments as dissolved silicate. Henceforth, we refer to dissolved silicate as silicate and particulate silicate as biogenic silica.

The flux of silicate through the Bering Strait is estimated to be 21 kmol s^{-1} from an average transport of 0.8 Sv (Coachman and Aagaard 1988) and an average silicate concentration of 25 μmol kg^{-1} obtained from climatologies (Garcia et al. 2006), consistent with concentrations reported for the Bering Strait area by Cooper et al. (1997). Eddies contribute an additional 5 kmol s^{-1} (Mathis et al. 2007). The contribution of biogenic silica is assumed to be negligible.

Riverine silicate inputs to the Arctic are estimated as 12 kmol s^{-1} from river discharges presented in Dittmar and Kattner (2003) and their mean silicate concentration of 150 mmol m^{-3}. Riverine inputs to the North Atlantic Ocean between the Arctic and 36°N are estimated to total 20 kmol s^{-1} (Table 3) from average silicate and biogenic silica concentrations of 150 and 28 mmol m^{-3}, respectively (Treguer et al. 1995; Conley 1997), and river flows of Howarth et al. (1996).

Mean downward biogenic silica fluxes in the Northeast Atlantic at the Porcupine Abyssal Plain (PAP) site (48°N, 20°W) are 63 mmol m^{-2} yr^{-1} (Ragueneau et al. 2001) and 115 mmol m^{-2} yr^{-1} at 38°–45°N, 16°–22°W (Mosseri et al. 2005). Scaling these values by the area of the Atlantic north of 36°N (approximately 3.7×10^7 km^2) gives downward fluxes of 74–135 kmol s^{-1}. The return flux of silicate from deep-ocean sediments to the water

TABLE 3. Silicate and biogenic silica riverine fluxes to the North Atlantic Ocean. River flows are from Howarth et al. (1996). Silicate and biogenic silica fluxes were estimated using these water discharge rates and reported mean riverine silicate (Treguer et al. 1995) and biogenic silica (Conley 1997) concentrations.

	Water discharge 10^3 m^3 s^{-1}	Silicate flux kmol s^{-1}	Biogenic silica flux kmol s^{-1}
North Canadian rivers	40.0	6.0	1.1
St. Lawrence basin	25.4	3.8	0.7
Northeast coast of the United States	6.6	1.0	0.2
Baltic Sea	15.1	2.3	0.4
North Sea	12.0	1.8	0.3
Northwest European coast	12.0	1.8	0.3
Southwest European coast	3.5	0.5	0.1
Total	114.6	17.2	3.1

TABLE 4. Data resolution matrix for the solution.

Net salinity	Gulf Stream	Discovery Gap	Seine Abyssal Plain	Net silicate	
0.998	0.001	−0.028	−0.022	0.018	Net salinity
0.001	0.000	−0.002	−0.001	−0.004	Gulf Stream
−0.028	−0.002	0.509	−0.385	0.318	Discovery Gap
−0.022	−0.001	−0.385	0.698	0.249	Seine Abyssal Plain
0.018	−0.004	0.318	0.249	0.794	Net silicate

column is 57 mmol m^{-2} yr^{-1} at the PAP site (Ragueneau et al. 2001). Scaling this by a similar area leads to a silicate flux from sediments to the water column of ~67 kmol s^{-1}.

In total we estimate sources of silica to the Atlantic between 36°N and the Bering Strait to be in the range of −10 to 51 kmol s^{-1}. Assuming the box is in steady state, this implies a range of silicate fluxes across the 36°N transect between 10 kmol s^{-1} northward and 50 kmol s^{-1} southward. Hence, the silicate constraint is set to be −20 kmol s^{-1} with an uncertainty of 30 kmol s^{-1}.

The inverse, based on the methods of Wunsch (1996), is constructed as in McDonagh et al. (2008) as a matrix equation. The information about the geometry and properties in the calculation is contained in a matrix that has 118 columns, corresponding to unknown reference velocities between station pairs; the columns are weighted using the station pair area. The matrix has five rows corresponding to constraints; the rows are weighted using the uncertainty in the constraint.

c. Solution

We use a SVD to solve the inverse system. The system is solved at rank = 3; that is, three singular values are included in the solution. This is the lowest rank where all constraints are satisfied to within twice the uncertainty in that constraint. The posterior errors on the constraints, calculated using the method and assumptions of McIntosh and Rintoul (1997), are given in Table 1. The solution reference velocity is everywhere less than 2 cm s^{-1} and only exceeds 1 cm s^{-1} in one region (bold dashed line in Fig. 3a)—that is in the Seine Abyssal Plain east of the mid-Atlantic ridge, forced by the constraints on the deepest water in this basin (Tables 1 and 4 and section 3d). The depth invariant solution reference velocity (bold dashed line in Fig. 3a) is added to the initial velocity field (crosses in Fig. 3c) to give our solution velocity field (bold solid line in Fig. 3c).

d. Effect of the constraints on the solution

The implications of the constraints for the solution are summarized in the data resolution matrix (Table 4). The construction and interpretation of this matrix are detailed in Wunsch (1996, 165–166). The magnitude of the diagonal elements of the matrix reflects the importance of a constraint in determining the solution. An element of size one has a unit effect on the solution. It is also useful to consider the column average properties (Fig. 4) when understanding the importance of a constraint, as these are the properties on which the solution (or reference velocity) operates.

The net salinity constraint is the most important for this solution (diagonal element = 0.998 in Table 4). This constraint is almost equivalent to a net volume constraint, except there is some small variability in the column average salinity (thin black line in Fig. 4).

The net silicate constraint is the next most important constraint (diagonal element = 0.794 in Table 4). The column average silicate concentration (bold black line in Fig. 4) has more structure in it than the salinity; therefore, there is structure in the solution added by this constraint. The solution preferentially adds southward velocity where the column average silicate is high to offset the initial northward silicate flux of 206 kmol s^{-1} (Table 1). As the high column average silicate concentrations occur in the deep water, this constraint tends to increase the overturning.

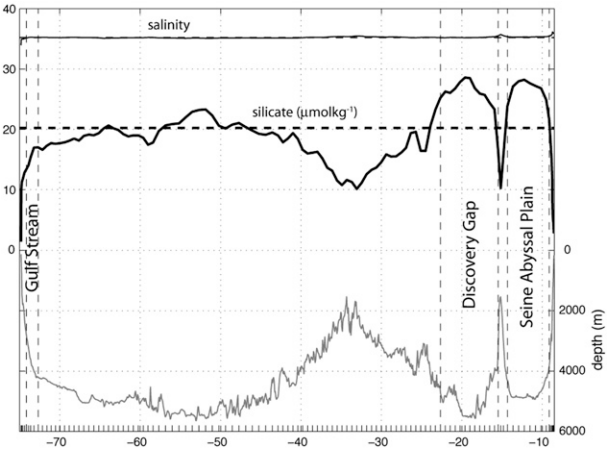

FIG. 4. Column average properties for salinity (solid thin line) and silicate (solid bold line). Section average salinity is 35.208 (dashed thin line) and section average silicate is 20.22 μmol kg^{-1} (dashed bold line). Solid gray line indicates the bathymetry on the section. Vertical dashed lines identify the stations included in the Gulf Stream, Discovery Gap, and Seine Abyssal Plain constraints as labeled.

The deep-water constraints in the Seine Abyssal Plain and Discovery Gap are the next most important constraints (diagonal elements = 0.698 and 0.509, respectively, in Table 4). These constraints, together with the net silicate, have the largest off-diagonal elements. In simple terms, when the solution adds a northward velocity in the Discovery Gap stations [to reduce the residual between the initial (−3.0 Sv) and constraint (0.3 Sv) transport there; Table 1 that have relatively high column average silicate concentrations] it adds a southward velocity across those stations that have the same high column average silicate values in the Seine Abyssal Plain to satisfy the net silicate constraint. Thus, these three constraints interact and result in the off-diagonal elements in Table 4.

The Gulf Stream constraint has little or no effect on the solution. This is the result of the Gulf Stream at this latitude being in deep water and the contrast of the column average properties being small between the Gulf Stream stations and other stations. This is not the same as the Gulf Stream being unimportant in the circulation; the Gulf Stream appears in the initial field and also appears (almost unchanged) in the final velocity field. We will see that the gyre circulation set up by the Gulf Stream is crucial in setting up the horizontal heat flux at this latitude.

4. Water masses and transport in temperature layers

We split the section into potential temperature classes to examine the circulation in each of those layers. The potential temperature interfaces, chosen to represent the boundaries between water masses, are based on those of Worthington (1976). Worthington included all of the deep and bottom water in a single layer cooler than 4°C. Here we split that single layer into 3 parts to differentiate between waters originating in the Antarctic (<1.8°C), the Nordic seas (1.8°–3°C), and the Labrador Sea (3°–5°C). We also raise the upper boundary of this deep water (from 4° to 5°C), so that both classic and upper Labrador Sea Waters (cLSW and uLSW, respectively; Pickart 1992) are included in a single layer. The thermocline waters are separated into upper thermocline waters warmer than 12°C, lower midthermocline waters at 7°–12°, and intermediate lower thermocline waters at 5°–7°C. These interfaces are shown in the section plots in Fig. 2 and in the property–property plots in Fig. 5.

The sense of the net transport in each of the temperature layers is the same in the solution as for the initial field (Table 2): northward flow in the lower, mid-, and upper thermocline layers warmer than 5°C; southward flow in the lower North Atlantic Deep Water (LNADW) and upper NADW (UNADW) layers between 1.8° and 5°C; and northward flow in the Antarctic Bottom Water (AABW) cooler than 1.8°C. In all of the layers, integrating from the west, the net flow is set by approximately 40°W, just west of the mid-Atlantic ridge crest; that is, although there is mesoscale variability in the flow east of 40°W, there is little net accumulation in the temperature layers other than at the eastern boundary east of 10°W (Fig. 6a).

a. AABW (cooler than 1.8°C)

Water of this temperature is only observed to the west of the mid-Atlantic ridge (Fig. 2a). This water is of Antarctic origin, as evidenced by the high values of deep silicate (Fig. 2d), and here we refer to it as AABW. The coldest potential temperature of 1.648°C and highest silicate value of 53.2 μmol kg^{-1} on the section were observed at the bottom of station 57 (53.9°W) at 5545 dbar. We chose 1.8°C as the upper limit of the AABW, as this is the point of a break in the slope in the potential temperature–salinity curve (Fig. 5c).

The solution has a net northward transport of AABW of 4.7 Sv (Table 2). A net northward transport of this water mass is realistic given its southern origin. The majority of the northward transport occurs between 56° and 51.9°W (16 Sv; Fig. 6c), centered on the coldest and most silicate rich water at 53.9°W. There is a southward recirculation to the west of this northward flow (−8.3 Sv) and small southward flows to the east of this northward flow (−2.2 Sv) and between 69° and 67°W (−0.8 Sv; Fig. 6c).

b. LNADW (between 1.8° and 3°C)

This water is ventilated in the Nordic seas and reaches the section via the deep overflows of the North Atlantic. We call this LNADW. West of the mid-Atlantic ridge, this layer is characterized by a maximum in oxygen (Figs. 2c and 5d). The highest oxygen values in the LNADW layer are at the western boundary, where concentrations in excess of 280 μmol kg^{-1} are observed at 3300 m (Figs. 2c and 5d). These oxygen concentrations are associated with the southward-flowing deep western boundary current that represents the most direct route of these waters from their formation regions to the 36°N section. East of the mid-Atlantic ridge, in the Madeira and Seine basins, the oxygen maximum associated with the LNADW is not present (Figs. 2c and 5d).

The DWBC transports 39% (4.5 Sv) of the net LNADW (11.7 Sv; Table 2) across the section in the solution. In total 12.5 Sv of this water are transported southward west of the MAR (Fig. 6). Although this temperature class exists in the eastern basin, it is unsurprising—given the lack of an oxygen maximum and the implied lack of recently ventilated LNADW—that the water east of the MAR is moving northward. The slight northward

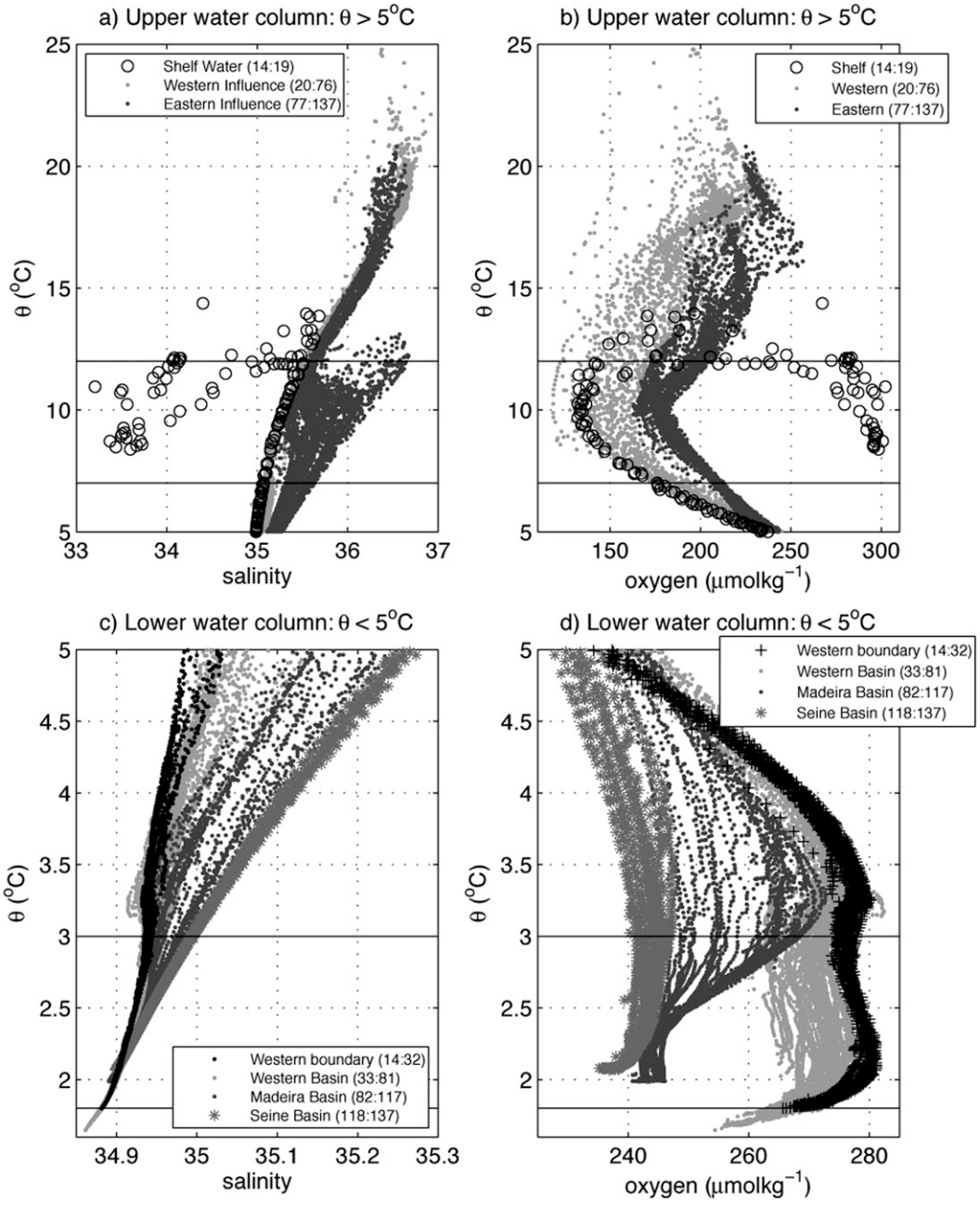

FIG. 5. (a),(c) Plots of $\theta-S$ and (b),(d) $\theta-O_2$ for (top) $\theta > 5$°C and (bottom) $\theta < 5$°C water columns along 36°N. Horizontal lines represent the water mass boundaries at 1.8°, 3°, 5°, 7°, and 12°C.

flow associated with the LNADW in the eastern basin is concentrated in the northward flow at the eastern boundary.

c. UNADW (between 3° and 5°C)

This layer contains cLSW and uLSW formed in the central and southern Labrador Sea, respectively. We call this water UNADW based on Pickart's (1992) analysis of the North Atlantic DWBC and we expect cLSW to lie between 3° and 4°C and the upper LSW (uLSW) to lie between 4° and 5°C. An oxygen maximum is observed between 3° and 4°C both west and east of the mid-Atlantic ridge (Figs. 2c and 5d). In the UNADW the highest oxygen concentrations and lowest salinity values are not observed at the western boundary; rather they are in the western basin near the mid-Atlantic ridge

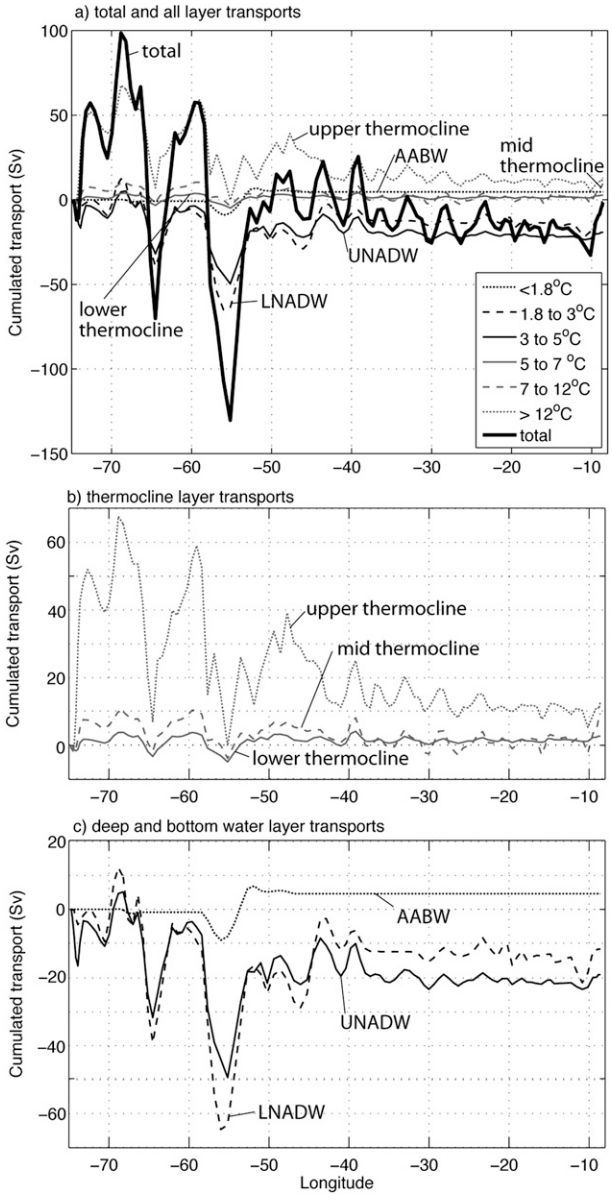

FIG. 6. Solution transport in potential temperature layers cumulated from the west (Sv): (a) all layers and total transport, (b) thermocline layers on an expanded transport scale, and (c) layers of deep and bottom water on an expanded transport scale.

(Figs. 5c and 5d). In the range of 3°–3.5°C, stations 63 and 66–72 at around 45°W have more extreme properties (particularly lower salinity) than the stations in the western boundary west of station 32. These western boundary stations sample the UNADW with the second highest oxygen and lowest salinity concentrations on the section.

The western boundary of this section lies to the south of the DWBC–Gulf Stream crossover. At this crossover Pickart and Smethie (1993) observed that much of the LSW in the DWBC is entrained into the Gulf Stream rather than continuing south in a DWBC. As part of CD171, we occupied a section at the western boundary to the north of the crossover at approximately 37°N. Even north of this crossover, the LSW has lower oxygen and higher salinity (i.e., less extreme properties; data not shown here) than in the interior on the 36°N around 45°W. The property distributions described here imply that the LSW that crosses the 36°N section near 45°W has not crossed the section before—that is, it is not recirculated. The more extreme LSW properties near 45°W (higher oxygen, lower salinity) further imply that the route that the LSW takes to 36°N, 45°W requires less modification and/or is more direct than the DWBC route to 36°N.

Of the 19.3-Sv southward flow in the UNADW (3°–5°C) layer (Table 2), 16.5 Sv flows southward in the DWBC between 74.8° and 73.8°W (Fig. 6c). Therefore, although the water properties suggest that there are pathways for the LSW (UNADW) to the 36°N section other than in the DWBC, the DWBC is the predominant route in terms of volume transport.

d. Lower thermocline (between 5° and 7°C)

Worthington (1976) included this water in the lower thermocline layer. The boundary at 7°C was chosen as no water colder than this passes from the Caribbean Sea into the Florida Strait. This layer has higher salinity and higher oxygen at the eastern end of the section than at the western end (Figs. 2a, 2b, 5a, and 5b). This difference is a maximum near the top of the layer at 7°C (Figs. 5a and 5b) and is likely the result of the influence of the overlying water masses, particularly the high salinity, high oxygen (relative to the other water at that temperature) Mediterranean water at the eastern end of the section. This layer varies the least in thickness across the section (Fig. 2) but changes its depth dramatically. This layer slopes down by 600 m underneath the Gulf Stream and then by an additional 700 m east of 40°W. This layer has a small (2.7 Sv) net northward transport across the section in the solution (Table 2).

e. Midthermocline (between 7° and 12°C)

This layer, described by Worthington (1976) as midthermocline water, shows substantial property variability along the section. At the western end of the section, this layer contains the shelf water, the freshest on the section, with salinities down to 33.36 (Fig. 2b). This layer also contains salinities of 36.64 associated with the Mediterranean water at the eastern end of the section (Fig. 2a). A significant increase in the thickness and salinity of this layer occurs, moving west to east, at 40°W,

which marks the western boundary of the direct influence of the Mediterranean water. This is also the approximate longitude where Worthington described the southward return of the Gulf Stream across 36°N. As well as exhibiting a vertical salinity maximum (Figs. 2b and 5a), the Mediterranean water is associated with a maximum in potential temperature (Figs. 2a and 5a) and a minimum in oxygen (Figs. 2c and 5b).

In the western basin (in the range of 74° and 40°W), between the shelf water to the west and Mediterranean water to the east, this layer has the lowest oxygen concentrations of the section (Figs. 2c and 5b). It is also associated with a vertical maximum in silicate (Fig. 2d). The maximum in silicate has been used to identify this water as Antarctic Intermediate Water (AAIW; Tsuchiya 1989). These extrema occur at 8°–9°C on this section, shallower and warmer than the 4°–5°C typically associated with AAIW in the South Atlantic (Talley 1996). The $\theta-S$ curve for these data shows no intermediate salinity minimum; however, there is a break in the slope of the western basin $\theta-S$ curve close to 9°C (Fig. 5a). We refer to this western basin water as midthermocline water; it has almost certainly been influenced by AAIW.

In the western boundary (west of 68.8°W), 9.9 Sv of this water flows northward (Fig. 6b). The majority of this flow recirculates between 68.8° and 40°W. East of 40°W, the cumulated flow changes with the mesoscale variability (with little net accumulation until the eastern boundary) around a value of 1–2 Sv (Fig. 6b). The mesoscale variability has a magnitude of ±(2–3) Sv in this layer. This implies that the recirculation between 68.8° and 40°W is 8–9 Sv. East of 10°W, there is a northward-flowing eastern boundary current of approximately 8 Sv (Fig. 6b). The estimate is approximate because it lies on a background of mesoscale variability. In summary, this solution gives a net northward flow of 1–2 Sv of the AAIW-influenced midthermocline west of 40°W and a northward flow of approximately 8 Sv of the Mediterranean-influenced midthermocline that is concentrated at the eastern boundary east of 10°W.

f. Upper thermocline and warm water (warmer than 12°C)

This layer includes 18° water that forms in the Sargasso Sea and is the subtropical mode water of the North Atlantic Ocean (Fig. 2a). This mode water is only observed to the east of the Gulf Stream. This layer contains Worthington's (1976) upper thermocline and warm-water layers. This upper thermocline layer has the classical shape of a subtropical gyre, deepening sharply across the western boundary and then gradually shallowing toward the eastern boundary. As with the lower thermocline layer (5°–7°C), the upper thermocline is generally more saline and higher in oxygen at the eastern end of the section than the western end (Figs. 5a and 5b); again, this is likely the influence of the Mediterranean water at the eastern end of the section.

There is some western boundary shelf water in this layer. This shelf water >12°C is a lens of water that is part of a temperature inversion that is approximately 100 m thick and a few tens of kilometers wide on this section (Fig. 5a). We also note that the potential temperature of some of the cores of Mediterranean outflow water exceed 12°C near the eastern boundary (Figs. 2a and 5a).

West of the mid-Atlantic ridge at 64° (centered at station 41), 57° (station 53), 55° (station 56), and 51°W (station 60), this layer is punctuated by low salinity values (Fig. 2b). The furthest west of these features is the most pronounced, with a surface salinity anomaly of −0.5 (Fig. 2b). The other three features have smaller surface salinity anomalies of between −0.1 and −0.15. The features, which have three discrete signatures in the surface water masses at 57°, 55°, and 51°W, appear as one mesoscale feature, centered at 55°W in the velocity field (solution velocity field in Fig. 3c). Hereinafter we will refer to two mesoscale features, one centered at 64°W and one centered at 55°W. Here, we note that the feature at 55°W has a more complex surface structure.

5. Circulation at 36°N

a. The overturning circulation

The solution has northward flow in the top 1170 m (Fig. 7a). The solution has an overturning (maximum northward flow transport field cumulated from the top down, including −2 Sv of surface Ekman flux) of 16.6 Sv at a depth of 1070 m (Fig. 7b). This represents an increase in strength and depth of the initial field overturning, 15.4 Sv at 1030 m. Beneath the upper-level northward flow, there are 2 lobes of southward-flowing deep water between approximately 1200 and 3000 m and between 3300 and 5000 m (Fig. 7a). The deeper of these lobes has been enhanced in the solution relative to the initial field (Fig. 7a). The result of this is a consistently southward flow between 1100 and 5000 m rather than the near-0-Sv transport that is evident between 3300 and 4500 m in the initial field (Figs. 7a and 7b). We interpret these two lobes of southward flow as the UNADW and LNADW. These southward-flowing deep waters overlie northward-flowing bottom water in the deepest 500 m (Figs. 7a and 7b).

We compared our solution for the overturning at this latitude with that of Macdonald (1998). While Macdonald does not explicitly give a value for the

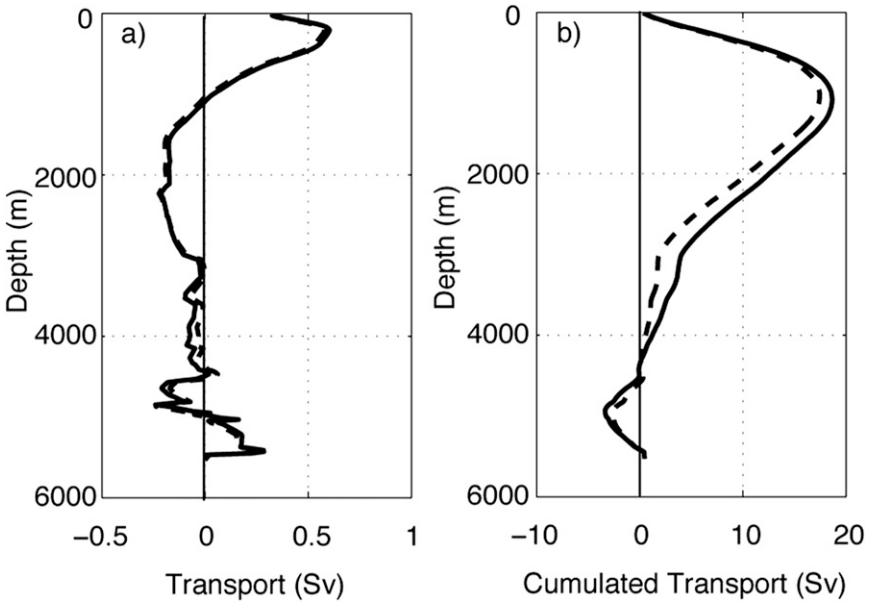

FIG. 7. Zonally integrated geostrophic transport across the section (Sv): (a) per 20-m bin and (b) cumulated from the top down, for the preferred solution (solid line) and the initial velocity field (dashed line). The Ekman flux (not shown) is −2 Sv in the top 20-m bin.

maximum overturning, her Table 12 reports 14×10^9 kg s^{-1} (approximately 14 Sv) of northward flow in the surface, thermocline and intermediate layers (her layers 1–6). Her solution is significantly different from ours because it has 7×10^9 kg s^{-1} (approximately 7 Sv) southward in the bottom water layers (average temperature of the upper layer boundary = 1.9°C), where we have 4.7 Sv northward of water colder then 1.8°C. The magnitude of this difference suggests that further detailed comparison between the two circulation schemes would not be fruitful.

b. The horizontal circulation

1) THE WESTERN BOUNDARY

West of 40°W the total flow is dominated by a northward-flowing Gulf Stream and accumulation of flow to nearly 100 Sv (the maximum in the western boundary flow) at 69°W as the track passes through the subtropical recirculation gyre (Fig. 6a). Details of the transport and solution velocity field at the western boundary are shown in Fig. 8. The southward transport of the DWBC is 22.6 Sv, which is defined as the cumulated southward transport deeper than 500 m (Fig. 8a). The DWBC is confined to the slope and underlies the core of the Gulf Stream, where surface velocities exceed 1.5 m s^{-1} (Fig. 8b). East of the DWBC, the Gulf Stream penetrates to the bottom. The Gulf Stream transport, 67.2 Sv, is integrated above 2000 m over the station pairs where the transport in the top 2 km is positive (Fig. 8a). East of the Gulf Stream, the total transport cumulates to a maximum of 98.5 Sv northward near 69°W (Fig. 8a). This transport, additional to the western boundary current (Gulf Stream) transport, is associated with the subtropical recirculation gyre.

2) EDDIES IN THE SUBTROPICAL GYRE

East of 69°W the southward return flow of the subtropical gyre is punctuated by two mesoscale features centered at 64° and 55°W. The feature at 64°W is associated with a negative salinity anomaly (discussed in section 4f) and has the sense of rotation for a cold-core ring shed from the Gulf Stream. The presence of a ring on the 36°N section at this longitude is confirmed by velocity fields from altimetry data (available online at http://rads.tudelft.nl/gulfstream/gif/gulf_050518_vel.gif). The other mesoscale feature in the velocity field is associated with three smaller salinity anomalies at 57°, 55°, and 51°W. This complex surface structure is also present in the altimetry velocity fields. In the solution transport field, the flow field associated with the three salinity anomalies appears to combine into one deep-reaching feature, centered at 55°W and of a similar size to the discrete ring at 64°W (Fig. 6a).

The two mesoscale features at 64° and 55°W are the largest signals in the cumulated transport field. The circulation associated with each of these features is of order 150 Sv (Fig. 6a). Taken in isolation the top-to-bottom southward flow in each of these mesoscale features is

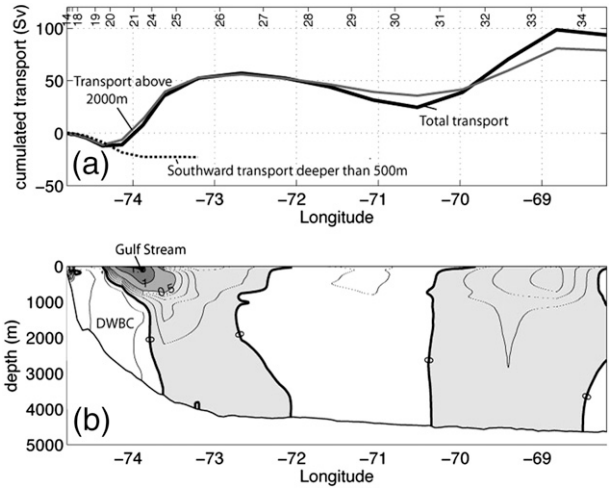

FIG. 8. (a) Transport (Sv) cumulated from the west at the western boundary for the top-to-bottom flow (bold line); flow above 2000 m (gray line); and southward transport deeper than 500 m (dotted line). (b) Solution velocity field (m s^{-1}) at the western boundary. Positive velocities (those with a northward component) are shaded. Dotted contours are at intervals of 0.1 between ± 0.5 m s^{-1}.

~50 Sv larger than the northward flow (Fig. 6a). However, we view these rings as two large features that sit on the background southward flow associated with the recirculation of the subtropical gyre. As such, these features are balanced and have little effect on the cumulated net flow outside of the rings. In terms of property fluxes, the combination of large volume fluxes and property contrasts that are associated with such discrete features give the potential for large uncertainties in the property fluxes if the features are not balanced. We expect that, as in the Indian Ocean subtropical gyre (McDonagh et al. 2008), our use of ADCP data to reference the initial velocity field greatly improves the representation and balance of these discrete mesoscale features.

3) THE SOUTHWARD RECIRCULATION OF THE GYRE

The Sverdrup relation predicts the transport associated with the interior recirculation that one would expect if the winds alone were forcing the subtropical gyre east of the western boundary. The Sverdrup transport at 36°N (shown in Fig. 9a) is calculated from the integrated meridional mass flux (M_y) divided by density, derived using the relation $\beta M_y = (\partial \tau_y/\partial x) - (\partial \tau_x/\partial y)$. The wind stresses τ_y, τ_x are from the National Oceanography Centre, Southampton (NOC) climatology (Josey et al. 1998), and β is the variation of Coriolis parameter with latitude.

The Sverdrup relation does not give the depth structure of the predicted transport, except that at the base of the wind-driven layer, the transport will be zero. ROW compared the Sverdrup transport with their circulation from the 1981 data using the transport above $\sigma_\theta = 27.4$. This isopycnal has an average depth of 830 m west of the Gulf Stream during CD171. Here we estimate the transports above 1000 and 2000 m to give a range of estimates for the flow to compare with the Sverdrup transport (Fig. 9a).

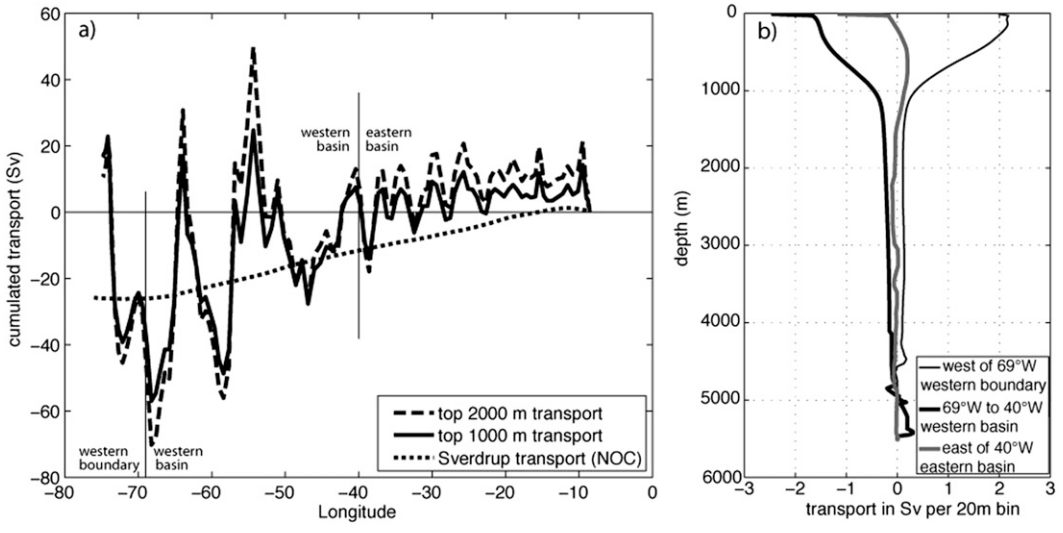

FIG. 9. (a) Solution transport (Sv) across the section above 2000 m (dashed line) and 1000 m (bold line) cumulated from east to west. Dotted line in (a) is theoretical transport from the Sverdrup relation calculated using the NOC wind climatology (Josey et al. 1998) cumulated from east to west. (b) Solution transport [Sv (20 m bin)$^{-1}$] across the western boundary (thin line); western basin (bold black line) and eastern basin (bold gray line).

The solution transport at 36°N does not look like the upper-level transport that one would expect if the winds (via the Sverdrup relation) alone were forcing the subtropical gyre east of the western boundary (Fig. 9a). ROW also found this to be true when they estimated the transport above $\sigma_\theta = 27.4$. The maximum southward transport associated with the interior (to the east of the western boundary) is 56.9 Sv (70.2 Sv) above 1000 (2000 m), more than the predicted Sverdrup transport of 25.9 Sv. Above 1000 (and 2000 m), the flow field east of the western boundary splits broadly into two regimes, one between 69° and 40°W (western basin) and the other from 40°W to the eastern boundary (eastern basin; Fig. 9a). Mesoscale variability makes it difficult to quantify the transport in each basin; however, in the eastern basin, the cumulated transport is less than the predicted Sverdrup transport and in the western basin the cumulated transport is more than the Sverdrup transport. Indeed, most of this northward flow occurs close to the eastern boundary. To the west of that northward flow, the accumulation of the solution transport (to within the mesoscale variability) follows the accumulation of the Sverdrup transport rather closely so that the dashed line sits approximately 10 Sv beneath the solid line between 10° and 40°W in Fig. 9a.

The depth-averaged transport (Fig. 9b) is less sensitive to the exact boundary chosen to split the western and eastern basins than the zonally cumulated transport in Fig. 9a. We expect the Sverdrup transport to be southward in each basin and decay to zero at some level near 1000 m—this happens in neither basin.

In the western basin between 40° and 69°W, there is a southward flow at all depth levels above 4000 m and there is still significant flow at 2000 m (Fig. 9b). We ascribe the difference between the Sverdrup transport and the observed transport to the Gulf Stream recirculation.

In the eastern basin between the eastern end of the section and 40°W, there is significant northward flow above 1000 m that reaches a maximum between 500 and 800 m. Above the maximum, the velocity goes to 0 m s^{-1}, only becoming southward in the top 100 m. That there is a surface southward flow is consistent with the progressive shoaling of the 17°C isotherm east of 40°W (Fig. 2a). That the flow is northward beneath this suggests that there is a process additional to the Sverdrup relation forcing the flow in the upper 1000 m. We suggest that this process is the thermohaline forcing in the Mediterranean and the northward flow of Mediterranean water across this part of the 36°N section.

4) THE EASTERN BOUNDARY

East of 10°W there is northward flow in all layers (Fig. 6a). The largest of these eastern boundary transports is in the 7°–12°C layer, which contains the Mediterranean water. However, we also see northward flow in the deep-water layers between 1.8° and 5°C. This full-depth northward flow is consistent with the current meter records of Meincke et al. (1975). Their mooring at 37°N and 9°53′W made measurements of mean northward currents at five depths through the water column in 2450 m of water. The data from this mooring contributed to the ''Evidence for a poleward eastern boundary current in the North Atlantic Ocean'' by J. C. Swallow et al. (1977, unpublished manuscript).

TABLE 5. Components of temperature, salinity, and silicate flux. Section average potential temperature, salinity, and silicate are 5.66°C, 35.208, and 20.22 μmol kg^{-1}, respectively.

	Temperature (Sv °C)	Salinity (Sv psu)	Silicate (kmol s^{-1})
Overturning (a)	183	17.14	−257
Horizontal (b)	97	10.95	299
Total (a + b) (no net transport)	280	28.09	42
Net throughflow (−1.55 Sv) (c)	−9	−54.52	−32
Total (a + b + c)	271	−26.44	10

6. Fluxes at 36°N

a. *Heat flux*

The solution velocity field has a temperature flux across the section of 271 Sv °C (Table 5). The solution corrected to zero net volume transport at the section average temperature of 5.66°C has a temperature flux of 280 Sv °C and a heat flux of 1.14 ± 0.12 PW northward. Following Hall and Bryden (1982), we split this into overturning and horizontal components of 0.75 PW (183 Sv °C) and 0.39 PW (97 Sv °C), respectively (Table 5). The overturning component is the product of the mean (on depth surfaces) temperature and volume flux. The horizontal component is the product of the residual from the mean (on depth surfaces) temperature and volume flux. The primary element of the overturning component is easily understood when one considers the overturning circulation is 16.6 Sv (section 5a) combined with a temperature contrast of approximately 10°C between the upper 1000 m and the deep water (Fig. 2a). The structure of the horizontal temperature flux is examined in Fig. 10 and described next.

West of 40°W, the horizontal temperature transport is dominated by the top 800 m (Fig. 10). Across the Gulf Stream and its recirculation to 69°W, there is a net positive transport of horizontal temperature flux. There appears to be no large net temperature transport associated

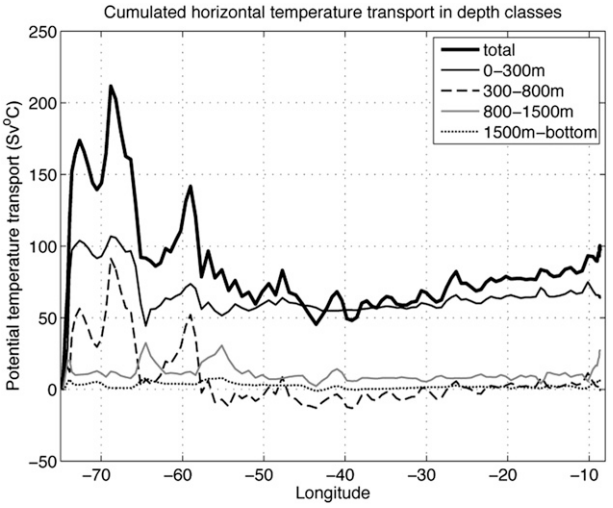

FIG. 10. Horizontal potential temperature transport in depth classes cumulated from the west (Sv °C).

with the rings at 64° and 55°W; that is, there is no step change in horizontal temperature transport across the rings, but rather there is a general decrease in transport associated with the southward return flow of the subtropical gyre and the transport associated with the rings superimposed on this flow.

East of 40°W, the cumulated horizontal temperature transport is positive. This cumulation comes in approximately equal part from the Mediterranean water (800–1500 m), with the dominant flow at the eastern boundary, and from the top 800 m, where a decreasing cumulated transport combines with a negative (on depth surfaces) temperature anomaly to give a positive cumulated horizontal temperature flux (Fig. 10). This decreasing cumulated transport is over a depth range rather than in the temperature classes shown in Fig. 6.

The magnitude of the net horizontal heat flux (0.39 PW) is similar to the difference between the RIW and ROW solutions. RIW mooted that the ROW smoothing removed the gyre component of the heat flux. Our results are consistent with that conjecture, that the horizontal heat flux is not in the eddy-like features but rather is in the western boundary flow, the interior flow associated with the gyre, and the northward flow of Mediterranean water at the eastern boundary.

b. *Freshwater flux*

The solution is constrained to have a salinity flux of -26.0 ± 5 Sv psu, the same as that at the Bering Strait using a 0.8-Sv Bering Strait throughflow at a salinity of 32.5. The solution has a net volume flux -1.55 ± 0.18 Sv (Table 2). Thus, assuming salt is conserved between the Bering Strait and 36°N, the divergence of freshwater between the Bering Strait and 36°N is 0.75 ± 0.24 Sv into the ocean. This is a larger input than the 0.33 Sv input of freshwater from the equivalent Talley (2008) analysis of the 1981 section. ROW and RIW did not report freshwater fluxes at 36°N.

c. *Flux uncertainties*

Wijffels (2001) presents an analysis of the errors associated with calculating the freshwater transport through a hydrographic section, and therefore the associated uncertainty in the divergence (precipitation − evaporation + runoff) between a section under analysis and a distant interbasin exchange (e.g., Bering Strait or the Indonesian Throughflow), assumed to be known. The freshwater, volume, or mass transport across a section can be calculated from an assumption about the salt transport. Since the uncertainty in the net transport of any other tracer depends in part on the uncertainty in the volume transport, we follow and extend Wijffels's analysis to consider the flux of any tracer across a hydrographic section. The details of this calculation are in the appendix.

7. Summary and discussion

Using data from a new transatlantic section at 36°N collected in 2005, we derive and describe a full-depth circulation field. Our initial velocity field is informed using bottom-tracked ADCP data. We find that the inclusion of ADCP data gives a more realistic initial field (in terms of coherence of the velocity structure and water mass transports) than traditional levels of no motion. We also find that the ADCP data improve our description of the mesoscale eddy field and reduce the flux uncertainties that are potentially associated with such features. The initial field is modified using inverse methods and constraints on circulation, net volume, and silicate fluxes. The net salinity and net silicate fluxes are the most significant constraints in terms of determining the solution. The two deep flow constraints are less significant and the Gulf Stream constraint is the least important of the five constraints. This relative unimportance in terms of determining the solution is a result of the Gulf Stream lying in 3500 m of water and representing relatively low column average property contrasts with the rest of the section. While least important in terms of solving the inverse problem, the size of the Gulf Stream is very important in terms of setting the magnitude of the horizontal heat flux and thus the net heat flux across the section.

In our solution the DWBC (southward velocity deeper than 500 m) carries 22.6 Sv. The DWBC is overlain by and inshore of the Gulf Stream at this latitude. The DWBC is trapped against the continental

shelf by the component of the Gulf Stream that penetrates to the bottom at this latitude. The Gulf Stream transport over the top 2000 m is 67.2 Sv. The solution has an overturning of 16.6 Sv at 1070 m. The horizontal circulation is dominated by the transport at the western boundary (reaches a top-to-bottom maximum of nearly 100 Sv northward at 69°W) and the southward recirculation across the rest of the gyre. West of 40°W, the upper-level circulation exceeds that predicted by the Sverdrup transport. A quantitative comparison is hampered by the mesoscale variability in the western basin. Two large mesoscale features (cold-core rings) are evident at 64° and 55°W. East of 40°W, the cumulation of the upper-level transport appears to match the Sverdrup transport more closely than in the western basin. In addition to the Sverdrup transport in the eastern basin is an approximately 10-Sv northward flow of Mediterranean water against the eastern boundary.

In terms of water mass properties, one striking result is the observation of two patches of recently ventilated UNADW on this 36°N section. We observe the recently ventilated UNADW (also called LSW) at the western boundary and in the interior, just west of the MAR, that has even more extreme properties, lower salinity, and higher oxygen. This interior pathway for LSW, with extreme properties comparable to those at the western boundary, was also mapped by Talley and McCartney (1982) using hydrographic data (see their Figs. 3 and 4). Although the UNADW with the most extreme properties lies in the interior (Figs. 5c and 5d), most (85%) of the recently ventilated UNADW crosses this section in the DWBC. This is apparently contrary to the float and modeling results of Bower et al. (2009), who found that only 0.1% of the e-floats (LSW-tracing floats simulated in a model) at 36°N did so continuously via the DWBC.

The key to the difference may be that the Lagrangian measures of the flow (real and virtual) used by Bower et al. (2009) require the flow to be continuous. Koltermann et al. (1999) discuss the presence of the interior pathway of LSW using hydrographic data and in the context of variability in the North Atlantic circulation and water properties. They conclude that the spreading of LSW property anomalies along the DWBC is as fast as—if not faster than—along the interior pathway (see their Fig. 4). However our observations show more extreme properties (implying more recent ventilation) in the interior pathway than at the DWBC. One interpretation of this is that mixing in the DWBC may be simultaneously eroding the extreme properties of the DWBC and ejecting floats, be they virtual or real from the DWBC. Lauderdale et al. (2008) showed mixing to be enhanced in the DWBC of Greenland. The assumption that deep flows should be any more continuous or steady than surface boundary flows may be what is causing the apparent contradiction between our results and those of Bower et al. (2009). Another interpretation is that the split between the interior and the DWBC route varies in time. We know that LSW properties vary, and Koltermann et al. (1999) strongly linked variability in the circulation to LSW production. However, we note that the presence of a deep western boundary current is consistently measured at all latitudes in the North Atlantic.

Our solution requires a southward freshwater flux of 1.55 ± 0.18 Sv across 36°N. To balance the implied oceanic divergence in freshwater would require a net input of freshwater of 0.75 Sv between 36°N and the Bering Strait.

The derived circulation has a heat flux of 1.14 ± 0.12 PW, most consistent with the RIW analysis of the 1981 box. The ROW analysis and also the global analysis of Talley (2003) give a lower heat flux across 36°N of 0.8 and 0.86 PW, respectively. These values of heat flux are close to our estimate of the overturning heat flux (0.75 PW). Thus, the difference between our estimate of the heat flux and the lower estimates is close to the horizontal heat flux of 0.39 PW. The horizontal heat flux in our circulation is primarily set by the gyre rather than the mesoscale variability observed on the section. Our observations of the heat flux are consistent with RIW's statement that the smoothing of ROW removed the gyre component of the heat flux.

Acknowledgments. We thank the scientists, technical staff, and crew of the RRS *Charles Darwin* during CD171 for collecting the data presented in this paper. The cruise and data analysis were supported by the NERC Consortium Grant NER/O/S/2003/00627. We also thank J. Alex Brearley for making the Sverdrup transport calculation. The comments of two anonymous reviewers have improved the manuscript, our thanks go to them.

APPENDIX

Estimation of Uncertainty in Tracer Flux Calculations

Suppose we have an observed velocity (v) field and a tracer concentration (C) field. Each can be written as the sum of a section area mean and its deviation. For this analysis we use Wijffels's (2001) Eq. (6.2.4), modified to be more precise by the explicit inclusion of density, ρ. We define: $v = \overline{v} + v'$; and $C = \overline{C} + C'$ where the mean values denoted by overbar are defined by

$$\overline{C} \iint \rho \, dx \, dz = \iint \rho C \, dx \, dz, \quad \text{so that} \quad \iint \rho C' \, dx \, dz = 0. \tag{A1}$$

Here, C could be any tracer or, for the purposes of defining $\overline{v}$, would be the velocity v.

Following Wijffels (2001) we use T_i^M for the interbasin mass transport and T_i^C for the interbasin tracer transport, and then $T_i^C = T_i^M C_i$, where C_i is the mean tracer concentration of the interbasin transport. Conservation of mass and tracer can now be written as

$$\int\int \rho v \, dx \, dz + (P - E + R) = T_i^M \quad \text{and} \tag{A2}$$

$$\int\int \rho v C \, dx \, dz + A + (P - E + R) \times C_{\text{PER}} = T_i^M C_i. \tag{A3}$$

Equation (A3) is an extension of Wijffels's (2001) Eq. (6.2.1) and allows for a source term (A) for the tracer (which could be from either the atmosphere or the seabed) and also allows precipitation (P), evaporation (E), and runoff (R) to have nonzero tracer concentrations (C_{PER}). Strictly, we could further allow a different tracer concentration for each of P, E, and R. Employing $C = \overline{C} + C'$ in Eq. (A3) and subtracting $\overline{C}$ times, Eq. (A2) gives

$$\int\int \rho v C' \, dx \, dz + A + (P - E + R) \times C'_{\text{PER}} = T_i^M C'_i. \tag{A4}$$

Further, we employ $v = \overline{v} + v'$, and noting that

$$\int\int \rho(\overline{v} + v')C' \, dx \, dz = \int\int \rho v' C' \, dx \, dz \tag{A5}$$

because the integral of the deviation C' is zero, we deduce

$$\int\int \rho v' C' \, dx \, dz + A + (P - E + R) \times C'_{\text{PER}} = T_i^M C'_i. \tag{A6}$$

For the particular case when the tracer is salt, Wijffels makes the reasonable simplification that A and C_{PER} are both zero. The latter requirement means that $C'_{\text{PER}} = -\overline{C}$, and Eq. (A6) can be rearranged to give

$$(P - E + R) = -\frac{T_i^M C'_i - \int\int \rho v' C' \, dx \, dz}{\overline{C}}, \tag{A7}$$

where C is now salt, which is the same as (6.2.5) in Wijffels (2001) because of Eq. (A5). Substituting for $(P - E + R)$ from (A7) in (A2), we recover the familiar result for the freshwater, volume, or mass flux through a section,

$$\int\int \rho v \, dx \, dz = \int\int \rho \overline{v} \, dx \, dz = \frac{T_i^M S_i - \int\int \rho v' S' \, dx \, dz}{\overline{S}}. \tag{A8}$$

The same result can be obtained directly from (A3) by choosing C to be salt, setting A and C_{PER} to zero, and expanding v and C into their mean and deviation parts.

Uncertainty analysis

To estimate the uncertainty in the total transport of a tracer across a section, we write it in the form of

$$\int\int \rho v C \, dx \, dz = \int\int \rho v' C' \, dx \, dz + \overline{C} \int\int \rho \overline{v} \, dx \, dz. \tag{A9}$$

First, consider the uncertainty in the mass flux from (A8). We refer to the uncertainty in the two terms in the numerator on the rhs of (A8) as e_1 and e_2, respectively. Combining the uncertainties in quadrature, the uncertainty e_3 in the mass flux [lhs of (A8)] is then

$$e_3 = \sqrt{e_1^2 + e_2^2}/\overline{S}. \tag{A10}$$

In (A9) we use e_6 for the uncertainty on the lhs (which is the net flux of tracer through a section) and assign uncertainties e_4 and e_5, respectively, to the two terms on the rhs.

Wijffels (2001) shows how to estimate an upper bound on e_2. We will use the same reasoning to estimate e_4, which is of the same form as e_2 but for a tracer other than salt, and e_5 is simply $\overline{C} \times e_3$. Therefore, the uncertainty on a tracer flux e_6 is given by

$$e_6 = \sqrt{e_4^2 + \frac{(e_1^2 + e_2^2)}{\overline{S}^2} \times \overline{C}^2}. \tag{A11}$$

To estimate e_2 Wijffels points out that for the purposes of oceanic flux calculations, v' and C' should be the long-term means of the relevant field. In practice the observed fields (either directly measured or inferred from a circulation analysis) differ from the long-term mean either because of measurement error or because of oceanic transients. Wijffels writes v' (and C') as the sum of the observed field v_o and its error v_e as

$$v' = v_o + v_e; \quad C' = C_o + C_e. \tag{A12}$$

Now considering only the first term on the rhs of (A9), the difference between the true tracer flux ($\iint \rho v' C' \, dx \, dz$) and that calculated from observations ($\iint \rho v_o C_o \, dx \, dz$) is given by the spatial correlation of the error terms in (A12):

TABLE A1. Mean values ($\overline{C}$), standard deviation along section (C_o), and estimates of measurement and other errors (C_e) for tracers measured during CD171; estimates of uncertainty from Eqs. (A11) (e_6) and (A13) (e_4). The difference between e_6 and e_4 is due to the uncertainty in volume transport through the Bering Strait. The values in columns e_4 and e_6 for salt and equivalent freshwater volume uncertainty are the values of e_2 and e_3 for those parameters. The equivalent freshwater volume uncertainty is the uncertainty in the salt flux divided by $\overline{S}$ = 35.208 g kg^{-1}. The value quoted for $\overline{S}$ is the average practical salinity, used as a mass fraction for the uncertainty calculations. The heat flux uncertainty e_4 in PW is obtained from the temperature flux e_4 for the zero-net-mass-flux part of the solution by making 1 PW equivalent to 245 Sv °C, so that $\rho c_p = 4.08 \times 10^6$ J m^{-3} °C^{-1}.

Tracer (concentration units, flux uncertainty units)	$\overline{C}$	C_o	C_e	e_4 (contribution to e_6 from measurement error or ocean transients)	e_6 (uncertainty in total transport of tracer across section)
Volume (Sv; N/A)	N/A	30	5	N/A	N/A
Salt (g kg^{-1}, 10^6 kg s^{-1})	35.208	0.49	0.1	3.9	6.3
Equivalent freshwater volume uncertainty (N/A; Sv)	N/A	N/A	N/A	0.11	0.18
Temperature (°C, Sv °C)	5.664	4.87	0.5	28.7	28.7
Heat (N/A; PW)	N/A	N/A	N/A	0.12	N/A
Silicate (μmol kg^{-1}, kmol s^{-1})	20.2	12.9	1	71.3	71.3

$$e_4 = \int\int \rho(v_e C_o + v_e C_e + v_o C_e)\, dx\, dz. \qquad \text{(A13)}$$

Ignoring errors or variations in density, an upper bound on e_4 is estimated by combining three error terms. Wijffels estimates the magnitude of v_e as equivalent to 5 Sv and v_o as 30 Sv. For the purposes of estimating magnitude, we will consider that practical salinity (dimensionless) is approximately equal to the dissolved salt mass fraction in grams per kilogram. The magnitude of C_o is the variability of the tracer along the section: Wijffels uses 1 g kg^{-1} for salinity; we use the standard deviation across our section, which is 0.49 g kg^{-1}. The C_e term is the magnitude of measurement error for the tracer: Wijffels uses 0.1 g kg^{-1} for salinity; we use the same value. To estimate the total error in tracer fluxes, we keep the same values as Wijffels for the velocity uncertainty, and Table A1 gives the magnitudes for the tracer uncertainties and the uncertainty in each total tracer flux. We use

$$e_1 = \text{error}_{T_i^M S_i} = 5 \times 10^9 \,\text{kg s}^{-1}$$

then

$$e_2 = (|5\,\text{Sv} \times 0.49\,\text{g kg}^{-1}| + |5\,\text{Sv} \times 0.1\,\text{g kg}^{-1}| + |30\,\text{Sv} \times 0.1\,\text{g kg}^{-1}|) \times 1000\,\text{kg m}^{-3},$$

so we estimate $e_2 = 3.9 \times 10^6$ g kg^{-1}.

We note that $e_5 = \overline{C} \times e_3$ is generally much smaller than e_4, because the uncertainty in volume flux at the Bering Strait is numerically small and $\overline{C}$ is not significantly larger than C'. This would not be the case when studying the flux of carbon parameters total inorganic carbon and total alkalinity, when the mean value is numerically much larger than the variability. For these two parameters, the uncertainty in the Bering Strait salt flux, e_1, will contribute significantly to the uncertainty in the total parameter flux across any single section, but not to the divergence between two sections that cross the same basin.

For silicate we take $C_e = 1$ μmol kg^{-1}. The C_e term is important where it is correlated with uncertainty in the velocity field; this is numerically largest in the upper ocean, where silicate values are low.

The values in the column e_6 thus indicate the order of magnitude of the uncertainty in the fluxes of each property, derived from some general assumptions about the magnitude of correlated imperfections in the velocity and tracer fields. They can be used either as a guide to the relative weights that should be assigned to different property constraints in the inverse procedure or as an indication of the uncertainty in the solution.

REFERENCES

Bower, A. S., M. S. Lozier, S. F. Gary, and C. W. Boning, 2009: Interior pathways of the North Atlantic meridional overturning circulation. *Nature,* **459,** 243–247.

Coachman, L. K., and K. Aagaard, 1988: Transports through the Bering Strait: Annual and interannual variability. *J. Geophys. Res.,* **93** (C12), 15 535–15 539.

Conley, D. J., 1997: Riverine contribution of biogenic silica to the oceanic silica budget. *Limnol. Oceanogr.,* **42,** 774–777.

Cooper, L. W., T. E. Whitledge, J. M. Grebmeier, and T. Weingartner, 1997: The nutrient, salinity, and stable oxygen isotope composition of Bering and Chukchi Seas waters in and near the Bering Strait. *J. Geophys. Res.,* **102** (C6), 12 563–12 573.

Dittmar, T., and G. Kattner, 2003: The biogeochemistry of the river and shelf ecosystem of the Arctic Ocean: A review. *Mar. Chem.,* **83,** 103–120.

Dobroliubov, S. A., 1997: Freshwater transport in the North Atlantic Ocean: Intercomparison of balance and direct estimates. Preprints, *22nd General Assembly on Intercomparison and*

Validation of the Ocean-Atmosphere Flux Field, Vienna, Austria, European Geophysical Society, 15 (Suppl. 2), Abstract OA8, p. C405.

Egbert, G., A. Bennett, and M. Foreman, 1994: TOPEX/Poseidon tides estimated using a global inverse model. *J. Geophys. Res.,* **99** (C12), 24 821–24 852.

Garcia, H. E., R. A. Locarnini, T. P. Boyer, and J. I. Antonov, 2006: *Nutrients (phosphate, nitrate, silicate)*. Vol. 4, *World Ocean Atlas 2005,* NOAA Atlas NESDIS 64, 396 pp.

Grist, J. P., and S. A. Josey, 2003: Inverse analysis adjustment of the SOC air–sea flux climatology using ocean heat transport constraints. *J. Climate,* **16,** 3274–3295.

Halkin, D., and T. Rossby, 1985: The structure and transport of the Gulf Stream at 73°W. *J. Phys. Oceanogr.,* **15,** 1439–1452.

Hall, M. M., and H. L. Bryden, 1982: Direct estimates and mechanisms of ocean heat transport. *Deep-Sea Res.,* **29A,** 339–359.

Hellerman, S., and M. Rosenstein, 1983: Normal monthly wind stress over the World Ocean with error estimates. *J. Phys. Oceanogr.,* **13,** 1093–1104.

Howarth, R. W., and Coauthors, 1996: Regional nitrogen budgets and riverine N & P fluxes for the drainages to the North Atlantic Ocean: Natural and human influences. *Biogeochemistry,* **35,** 75–139.

Josey, S. A., E. C. Kent, and P. K. Taylor, 1998: *The Southampton Oceanography Centre (SOC) Ocean-Atmosphere Heat, Momentum and Freshwater Flux Atlas*. Southampton Oceanography Centre Rep. 6, 30 pp.

——, ——, and ——, 1999: New insights into the ocean heat budget closure problem from analysis of the SOC air–sea flux climatology. *J. Climate,* **12,** 2856–2880.

Koltermann, K. P., A. V. Sokov, V. P. Tereschenkov, S. A. Dobroliubov, and A. Sy, 1999: Decadal changes in the thermohaline circulation of the North Atlantic. *Deep-Sea Res. II,* **46,** 109–138.

Lauderdale, J. M., S. Bacon, A. C. Naveira Garabato, and N. P. Holliday, 2008: Intensified turbulent mixing in the boundary current system of southern Greenland. *Geophys. Res. Lett.,* **35,** L04611, doi:10.1029/2007GL032785.

Lavin, A. M., H. L. Bryden, and G. Parrilla, 2003: Mechanisms of heat, freshwater, oxygen and nutrient transports and budgets at 24.5°N in the subtropical North Atlantic. *Deep-Sea Res. I,* **50,** 1099–1128.

Macdonald, A. M., 1998: The global ocean circulation: A hydrographic estimate and regional analysis. *Prog. Oceanogr.,* **41,** 281–382.

Mathis, J. M., R. S. Pickart, D. A. Hansell, D. Kadko, and N. R. Bates, 2007: Eddy transport of organic carbon and nutrients from the Chukchi Shelf: Impact on the upper halocline of the western Arctic Ocean. *J. Geophys. Res.,* **112,** C05011, doi:10.1029/2006JC003899.

McDonagh, E. L., and Coauthors, 2007: RRS *Charles Darwin* Cruise CD171, 01 May - 15 Jun 2005: A trans-atlantic hydrographic section at 36°N. National Oceanography Centre, Southampton Cruise Rep. 14, 127 pp.

——, H. L. Bryden, B. A. King, and R. J. Sanders, 2008: The circulation of the Indian Ocean at 32°S. *Prog. Oceanogr.,* **79,** 20–36.

McIntosh, P. C., and S. R. Rintoul, 1997: Do box inverse models work? *J. Phys. Oceanogr.,* **27,** 291–308.

Meincke, J., G. Siedler, and W. Zenk, 1975: Some current observations near the continental slope off Portugal. *''Meteor'' Forschungsergeb.,* **A16,** 15–22.

Mosseri, J., B. Quéguiner, P. Rimmelin, N. Leblond, and C. Guieu, 2005: Silica fluxes in the northeast Atlantic frontal zone of Mode Water formation (38°–45°N, 16°–22°W) in 2001–2002. *J. Geophys. Res.,* **110,** C07S19, doi:10.1029/2004JC002615.

Pickart, R. S., 1992: Water mass components of the North Atlantic Deep Western boundary current. *Deep-Sea Res.,* **39,** 1553–1572.

——, and W. M. Smethie Jr., 1993: How does the deep western boundary current cross the Gulf Stream? *J. Phys. Oceanogr.,* **23,** 2602–2616.

Ragueneau, O., and Coauthors, 2001: The benthic silica cycle in the Northeast Atlantic: Annual mass balance, seasonality, and importance of non-steady-state processes for the early diagenesis of biogenic opal in deep-sea sediments. *Prog. Oceanogr.,* **50,** 171–200.

Reid, J. L., 1994: On the total geostrophic circulation of the North Atlantic Ocean: Flow patterns, tracers and transports. *Prog. Oceanogr.,* **33,** 1–92.

Rintoul, S. R., and C. Wunsch, 1991: Mass, heat, oxygen and nutrient fluxes and budgets in the North Atlantic Ocean. *Deep-Sea Res.,* **38** (Suppl. 1), S355–S377.

Roemmich, D., and C. Wunsch, 1985: Two transatlantic sections: Meridional circulation and heat flux in the subtropical North Atlantic Ocean. *Deep-Sea Res.,* **32,** 619–624.

Sato, O. T., and T. Rossby, 2000: Seasonal and low-frequency variability of the meridional heat flux at 36°N in the North Atlantic. *J. Phys. Oceanogr.,* **30,** 606–621.

Saunders, P. M., 1987: Flow through Discovery Gap. *J. Phys. Oceanogr.,* **17,** 631–643.

Talley, L. D., 1996: Antarctic Intermediate Water in the South Atlantic. *The South Atlantic: Present and Past Circulation,* G. Wefer, et al., Eds., Springer-Verlag, 219–238.

——, 2003: Shallow, intermediate, and deep overturning components of the global heat budget. *J. Phys. Oceanogr.,* **33,** 530–560.

——, 2008: Freshwater transport estimates and the global overturning circulation: Shallow, deep and throughflow components. *Prog. Oceanogr.,* **78,** 257–303, doi:10.1016/j.pocean.2008.05.001.

——, and M. S. McCartney, 1982: Distribution and circulation of Labrador Sea Water. *J. Phys. Oceanogr.,* **12,** 1189–1205.

Taylor, P. K., 2000: Intercomparison and validation of ocean–atmosphere energy flux fields. Final Rep. of the Joint WCRP/SCOR Working Group on Air–Sea Fluxes, WCRP-112, WMO/TD-1036, 306 pp.

Treguer, P., D. M. Nelson, A. J. Van Bennekom, D. J. DeMaster, A. Leynaert, and B. Queguiner, 1995: The silica balance in the world ocean: A reestimate. *Science,* **268,** 375–379.

Trenberth, K. E., and J. M. Caron, 2001: Estimates of meridional atmosphere and ocean heat transports. *J. Climate,* **14,** 3433–3443.

Tsuchiya, M., 1989: Circulation of the Antarctic Intermediate Water in the North Atlantic Ocean. *J. Mar. Res.,* **47,** 747–755.

Wijffels, S., 2001: Ocean transport of fresh water. *Ocean Circulation and Climate,* G. Siedler, J. Church, and J. Gould, Eds., Academic Press, 475–488.

Woodgate, R. A., K. Aagaard, and T. J. Weingartner, 2005: Monthly temperature, salinity, and transport variability of the Bering Strait through flow. *Geophys. Res. Lett.,* **32,** L04601, doi:10.1029/2004GL021880.

Worthington, L. V., 1976: *On the North Atlantic Circulation*. The Johns Hopkins Oceanographic Studies, Vol. 6, John Hopkins University Press, 110 pp.

Wunsch, C., 1996: *The Ocean Circulation Inverse Problem*. Cambridge University Press, 442 pp.